Materials Science & Engineering A 832 (2022) 142440

Contents lists available at ScienceDirect

Materials Science & Engineering A

journal homepage: www.elsevier.com/locate/msea

Enhanced tensile properties by heterogeneous grain structures and coherent precipitates in a CoCrNi-based medium entropy alloy

Zihan Zhang [a,b], Ping Jiang [a], Fuping Yuan [a,b,*], Xiaolei Wu [a,b]

[a] State Key Laboratory of Nonlinear Mechanics, Institute of Mechanics, Chinese Academy of Science, 15 Beisihuan West Road, Beijing, 100190, China
[b] School of Engineering Science, University of Chinese Academy of Sciences, 19A Yuquan Road, Beijing, 100049, China

ARTICLE INFO

Keywords:
High entropy alloys
Heterogeneous structures
Precipitates
Strain hardening
Strengthening
Ductility

ABSTRACT

A dual heterogeneous structure with both heterogeneous grain structure and coherent $L1_2$ nanoprecipitates was obtained in a CoCrNi-based medium entropy alloy (MEA) with chemical composition of Co34.5Cr32-Ni27.5Al3Ti3 (in at%). The volume fraction of $L1_2$ phase is observed to become higher and the corresponding interspacing becomes smaller after aging, resulting in a more severe heterogeneity. The unaged samples are found to have better tensile properties as compared to those for the CoCrNi MEA with homogeneous and heterogeneous grain structures. The aged samples display an even better synergy of strength and ductility than the corresponding unaged samples. The hetero-deformation-induced hardening plays a more important role in the aged samples than in the unaged samples, especially at the elasto-plastic transition stage, producing higher density of geometrically necessary dislocations for better tensile properties. Multiple deformation twins, stacking faults and Lomer-Cottrell locks are the dominant deformation mechanisms for the unaged samples, while interactions between these defects and $L1_2$ nanoprecipitates play important roles in the aged sample, the shearing hardening mechanism is observed for $L1_2$ nano-particles.

1. Introduction

High-entropy alloys (HEAs) [1–11] and medium-entropy alloys (MEAs) [12–26] are a new class of materials which have attracted extensive research interests due to their excellent mechanical properties. HEAs and MEAs are generally composed of multiple principal elements (three or more) with nearly equal molar fraction. HEAs and MEAs generally have a single phase solid solution, for example, FCC FeCrMnCoNi HEA [1–5,11] and CoCrNi MEA [12–17,19–22,24] have drawn significant attentions recently due to their excellent tensile properties and extraordinary fracture toughness under room temperature, and even better tensile properties and toughness under cryogenic temperature due to a transition of the dominant deformation mechanism from dislocation behaviors to deformation twins [4,12].

The structural applications of HEAs and MEAs with coarse grains (CGs) are limited due to their relatively low yield strength although they have extraordinary ductility and toughness as compared to the other metals and alloys [4,12,13,19]. The yield strength of HEAs and MEAs can usually be elevated by grain refinement through severe plastic deformation or cold working [27]. However, such strength elevation in homogeneous structures is inevitably accompanied with reduction of ductility [28]. This strength-ductility trade-off in homogeneous structures can be evaded by heterogeneous structures [29–33]. The extra strain hardening mechanisms in heterogeneous structures can be attributed to the strain gradients and geometrically necessary dislocations (GNDs) induced by the deformation incompatibility among different domains with dramatic different mechanical properties [31]. Hetero-deformation induced (HDI) hardening and stress/strain partitioning have been found to play important roles during tensile testing in the HEAs and MEAs with heterogeneous grain structures, resulting in an extraordinary synergy of strength and ductility [31–33].

The yield strength of metals and alloys can be elevated by other ways, besides grain refinement and cold working, such as hard second-phase particles [34,35], while the ductility in such alloys is generally sacrificed due to the stress concentration and the early crack initiation around the hard second-phase particles. However, excellent tensile properties can be effectively achieved by coherent nanoprecipitates in alloys [36,37] due to the diminished lattice misfit and the alleviated stress concentration at phase interfaces. Such strategy by tailoring microstructures has been successfully applied to HEAs and MEAs recently

* Corresponding author. State Key Laboratory of Nonlinear Mechanics, Institute of Mechanics, Chinese Academy of Science, 15 Beisihuan West Road, Beijing, 100190, China.
E-mail addresses: zhangzihan@imech.ac.cn (Z. Zhang), jping@imech.ac.cn (P. Jiang), fpyuan@lnm.imech.ac.cn (F. Yuan), xlwu@imech.ac.cn (X. Wu).

https://doi.org/10.1016/j.msea.2021.142440
Received 3 September 2021; Received in revised form 1 November 2021; Accepted 29 November 2021
Available online 2 December 2021

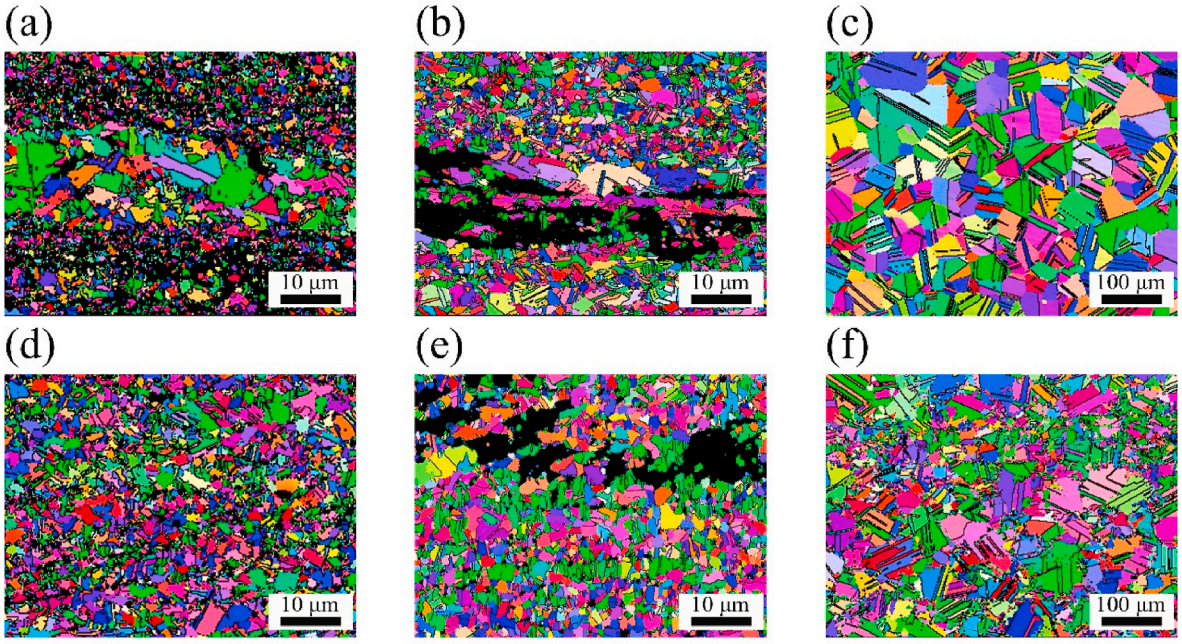

Fig. 1. EBSD observations for selected samples prior to tensile testing. IPF images for the unaged samples: (a) the CRA850 sample; (b) the CRA900 sample; (c) the CRA1000 sample. IPF images for the aged samples: (d) the CRAA850 sample; (e) the CRAA900 sample; (f) the CRAA1000 sample.

to evade the strength-ductility dilemma [38–47]. These formed coherent nanoprecipitates can provide additional Orowan's strengthening/hardening for achieving better tensile properties in HEAs and MEAs, besides minimizing the misfit strain and alleviating the stress concentration. Running dislocations will inevitably hit the coherent nanoprecipitates and be blocked (bow-out or cutting mechanisms) for Orowan's strengthening/hardening, and the Orowan's strengthening/hardening is highly dependent on the size and interspacing of the coherent nanoprecipitates.

Since both heterogeneous grain structures and coherent nanoprecipitates have benefits on the tensile properties of HEAs and MEAs, thus a dual heterogeneous microstructure with both heterogeneous grain structures and coherent nanoprecipitates has great potential opportunity to achieve extraordinary tensile properties. The potential extra strain hardening/strengthening effects of these two heterogeneous structures on the tensile behaviors should be carefully investigated and revealed for the samples with a dual heterogeneous microstructure. In this regard, the samples with a dual heterogeneous microstructure, have been fabricated in a Co–Cr–Ni-based MEA ($Co_{34.46}Cr_{32.12}Ni_{27.42}Al_3Ti_3$, in at%) by cold rolling (CR) followed by different heat treatments (annealing and aging). Then, the tensile properties and the corresponding microstructural mechanisms for the samples with dual heterogeneous microstructures have been studied and compared with data for the samples of the CoCrNi MEA with homogeneous and heterogeneous grain structures from the previous research [12,14,15], and then the effects of heterogeneous grain structures and coherent nanoprecipitates, and the possible extra strain hardening/strengthening effects on the mechanical properties have been revealed.

2. Materials and experimental techniques

The Co–Cr–Ni-based MEA ($Co_{34.46}Cr_{32.12}Ni_{27.42}Al_3Ti_3$, in at%) was first melted by electromagnetic levitation under a high-purity argon atmosphere, and then cast into ingots. The ingots were then homogenized at 1200 °C for 2 h in a vacuum environment, and then hot-forged into plates with a thickness of 10 mm with a starting temperature of 1150 °C. The hot-forged plates were then annealed again at 1200 °C for 2 h in a vacuum environment followed by water quenching, and then the plates were conducted a multi-pass CR process (0.16 mm thickness reduction per rolling) with a total reduction ratio up to 90%. The CR samples were then annealed at various temperatures (800, 850, 900, 950, 1000 °C) for 1 h followed by water quenching. Then, the annealed samples were also isothermally aged at 700 °C for 4 h followed by water quenching. The samples with homogeneous grain size and coherent nanoprecipitates were obtained by annealing at high temperatures (1000 °C) followed by aging, while the samples with a dual heterogeneous microstructure were fabricated by annealing at intercritical temperatures (800, 850, 900 °C) followed by aging. The annealed samples are referred as CRA800, …, while the aged samples are named as CRAA800, …, for convenience.

The plated dog-bone shaped specimens with gauge section dimensions of 15 × 5.5 × 3.3 mm^3 were utilized for quasi-static tensile testing. The quasi-static uniaxial tensile tests, load-unload-reload (LUR) tests and stress-relaxation tensile tests have been conducted with displacement control using an Instron 5565 testing machine under a strain rate of 5×10^{-4}/s and under room temperature. The data repeatability has been insured by conducting three tests for each specimen and the error bars for the data has been provided. The tensile direction was selected to be parallel to the rolling direction. The specimens have been first elongated to various designated strains at a strain rate of 5×10^{-4}/s during LUR tests, then the specimens have been unloaded to 20 N at an unloading rate of 200 N/min with stress control, followed by reloading at the same strain rate. An extensometer has been utilized during both tensile tests and LUR tests to accurately measure and control the displacement. During stress-relaxation tensile tests, the specimens have been first stretched to pre-determined strains at a strain rate of 5 × 10–4/s, and then the strain was maintained while the stress was recorded as a function of time. After the first relaxation over an interval of 120 s, the specimen was reloaded by a strain increment of 2.0% at a strain rate of 1×10^{-4}/s for the next relaxation. Four stress relaxations were conducted at 0.5%, and then the specimen was strained to next strain at a strain rate of 5×10^{-4}/s. The relaxation and reloading cycles were then performed with the same testing parameters used at 0.5% for the following pre-determined strains. The method to calculate the mobile dislocation density can be found in our previous paper [48].

X-ray diffraction (XRD), energy disperse spectroscopy (EDS),

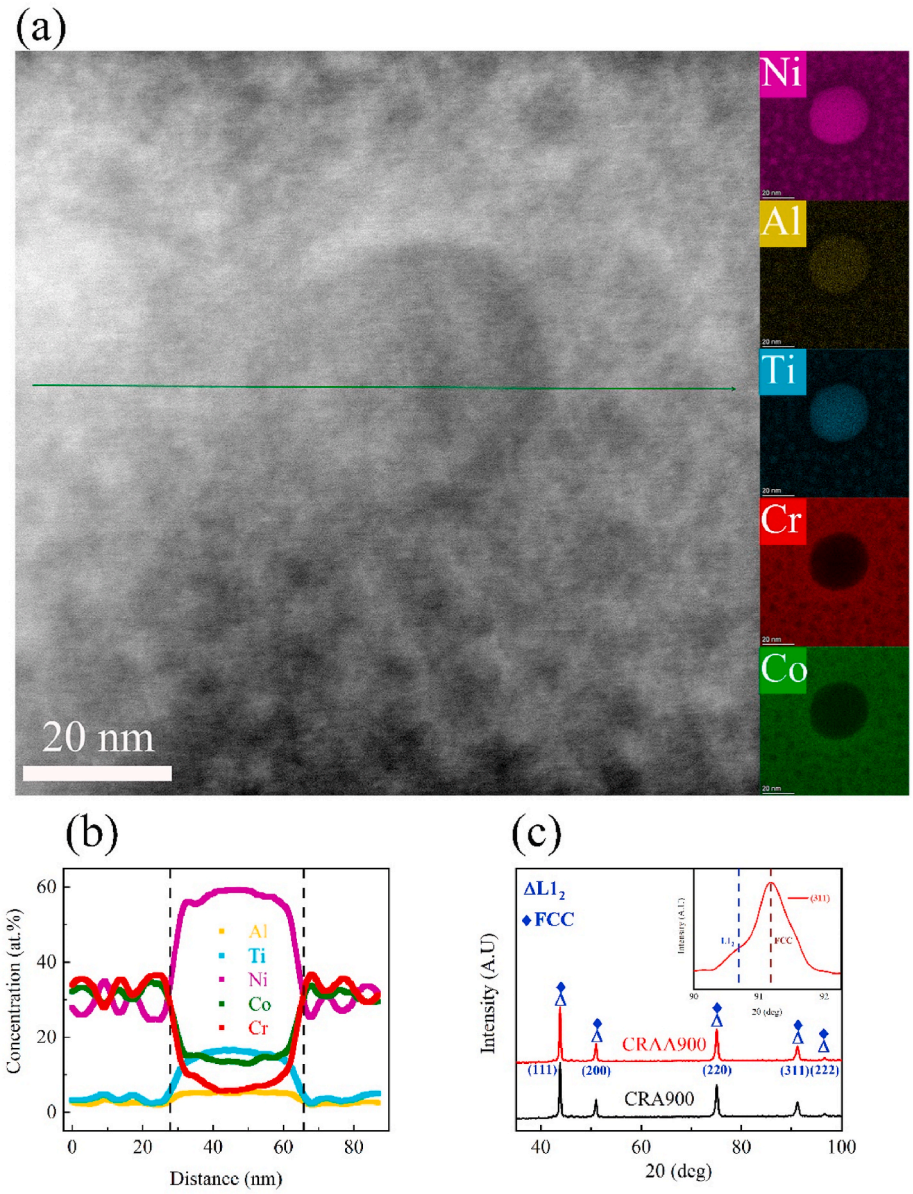

Fig. 2. (a) EDS mapping for an area with a $L1_2$ nano-particle. (b) Element distributions along the marked line in (a). (c) The XRD spectra for one typical unaged sample and one typical aged sample.

electron back-scattered diffraction (EBSD), back-scatter electron (BSE) microscopy, transmission electron microscopy (TEM), and high-resolution transmission electron microscopy (HRTEM) have been utilized to reveal the microstructures prior to and after tensile testing. The sample surfaces for EBSD have been carefully polished by a 0.05 μm SiO_2 aqueous suspension. The thin films for TEM observations have been mechanically polished down to about 50 μm, and then have been twin-jet perforated utilizing a solution of 5% perchloric acid and 95% ethanol at 248 K and 30 V. The minimum scanning step used for EBSD observation was 25 nm, and grain boundaries (GBs) have been only identified by misorientations larger than 15°. Kernel average misorientation (KAM) has been calculated against the first nearest neighbor ignoring the misorientation larger than 5°.

3. Results and discussions

The EBSD observations for selected samples prior to tensile testing are shown in Fig. 1, in which only high-angle GBs and twin boundaries (TBs) are shown. It is indicated previously that high-angle GBs and TBs are similar barriers in obstructing dislocation motion [49]. The inverse pole figures (IPF) for the annealed (unaged) samples are shown in Fig. 1a, b and 1c, respectively. The IPF for the corresponding aged samples are displayed in Fig. 1d, e and 1f, respectively. In Fig. 1a, b, 1d and 1e, only the recrystallized CGs are shown for clarity by blacking out the area for ultrafine grains (UFGs). It is clearly shown that the samples of CRA850, CRA900, CRAA850, and CRAA900 have a heterogeneous grain structure consisting of both un-recrystallized UFGs and recrystallized CGs. The area fractions of recrystallized CGs are 82.2%, 89.0%, 83.8%, and 91.3%, respectively, for these four samples. Moreover, the average grain sizes of recrystallized CGs are 2.7, 3.3, 1.5, and 3.0 μm, respectively, for these four samples. While, only recrystallized CGs are observed for the samples of CRA1000 and CRAA1000, indicating that these samples are fully recrystallized during annealing. Thus these two samples show a relatively homogeneous structure, and the average grain sizes are about 24.9 and 24.7 μm for these two samples, respectively. Annealing twins can also be observed in these two samples. The straight TBs are marked by black lines in Fig. 1. The average grain sizes of recrystallized grains for the aged samples are observed to be smaller

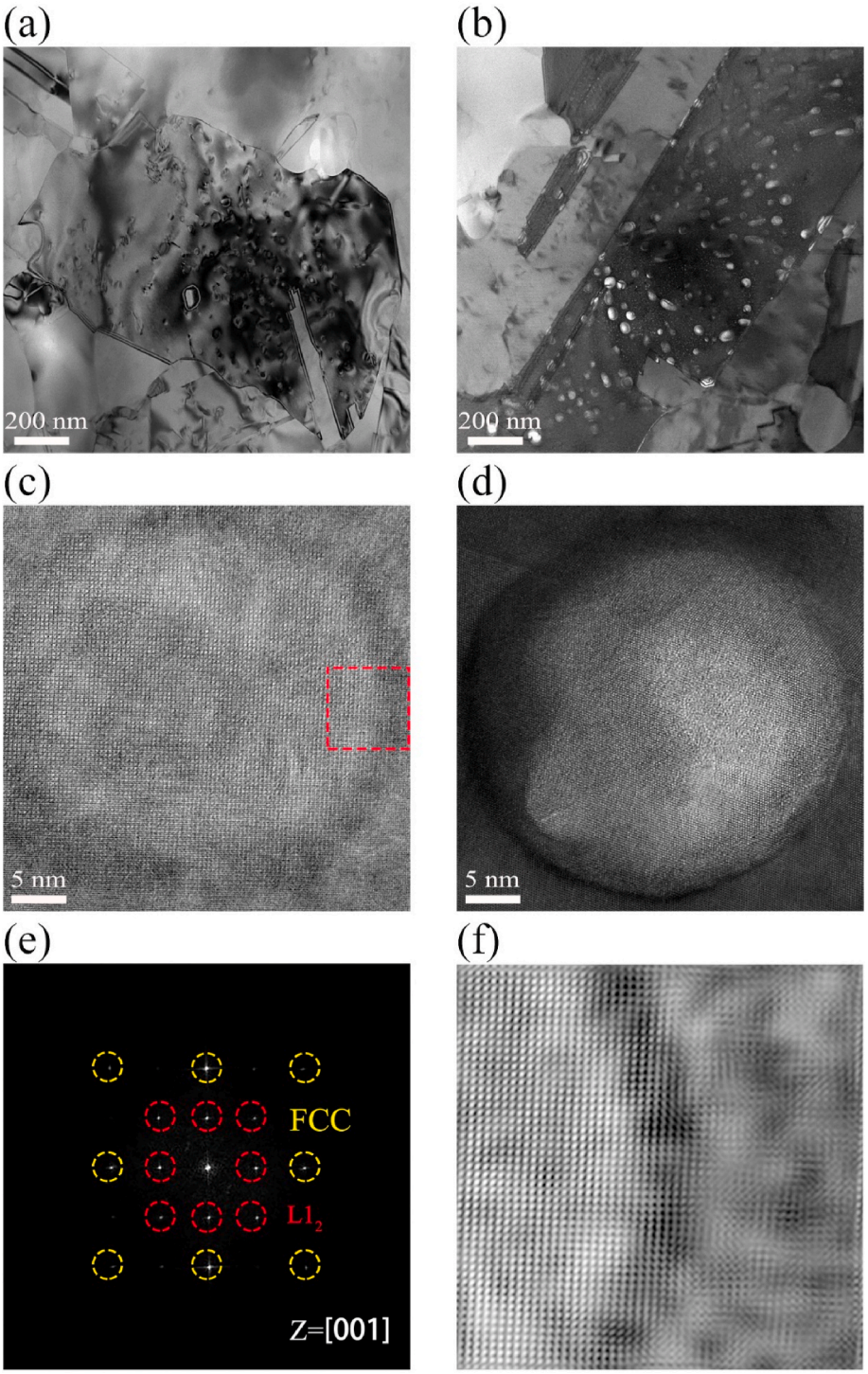

Fig. 3. TEM images for (a) one typical unaged sample and (b) one typical aged sample. HRTEM images showing $L1_2$ nanoprecipitates for (c) one typical unaged sample and (d) one typical aged sample. (e) The corresponding image after FFT for the marked rectangular area in (c). (f) The corresponding image after FFT and inverse FFT for the marked rectangular area in (c).

than those for the corresponding unaged samples due to the second recrystallization during aging at 700 °C (the average grain size for the second recrystallization is smaller than that for the first recrystallization).

The EDS mapping for an area with a $L1_2$ nano-particle is shown in Fig. 2a, while the element distributions along the marked line in Fig. 2a are displayed in Fig. 2b. As indicated, Ni, Ti and Al elements are enriched in the $L1_2$ nano-particle, while Cr and Co elements are deprived in the $L1_2$ nano-particle. In order to identify the phases for the unaged and aged samples, the XRD spectra for one typical unaged sample (CRA900) and one typical aged sample (CRAA900) are displayed in Fig. 2c. These peaks are observed to be asymmetric (indicated by the close-up view in the inset) due to co-existing of the FCC matrix and the $L1_2$ precipitates for both the unaged and aged samples. Since the $L1_2$ precipitates are coherent with the FCC matrix, each of the FCC diffraction peak is actually an overlap of those two phases.

TEM and HRTEM images for the typical unaged sample (CRA900) and the corresponding aged sample (CRAA900) are displayed in Fig. 3.

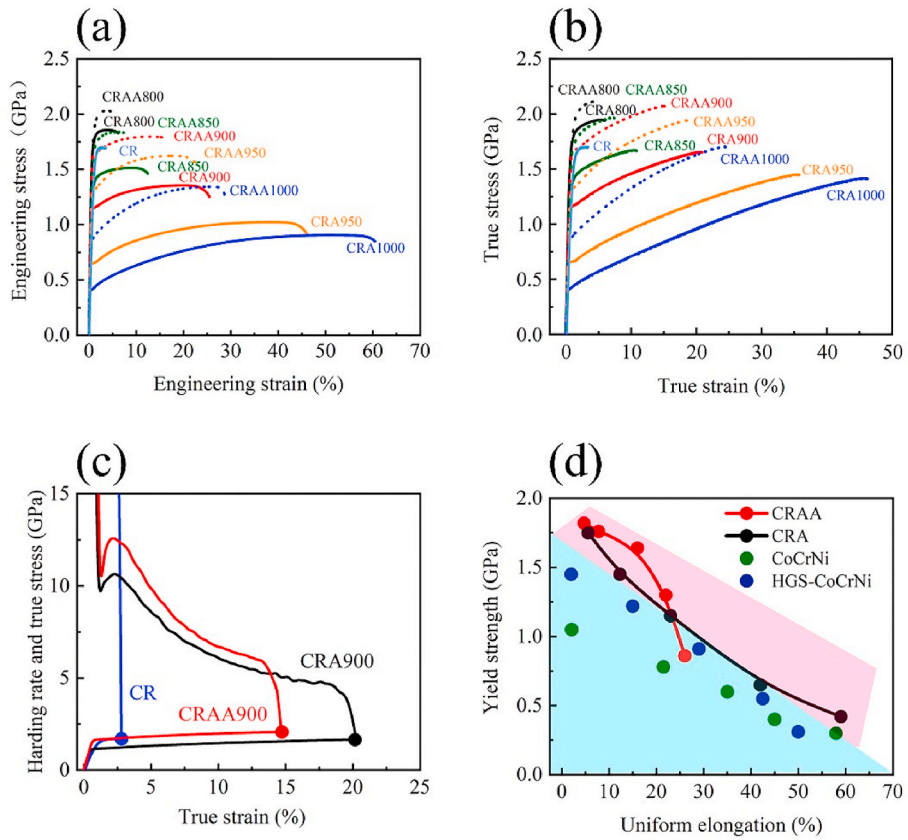

Fig. 4. Tensile properties for various samples. (a) Engineering stress-strain curves for various samples. (b) True stress-strain curves for various samples. (c) Θ as a function of true strain for one typical unaged sample and one typical aged sample. (d) Yield strength as a function of uniform elongation for all tested samples in the present study, the data for the CoCrNi MEA with both homogeneous [12,14] and heterogeneous grain structures [15] are also displayed for comparison.

$L1_2$ nano-particles can be found in both samples, while the interspacing is clearly smaller and the relative volume fraction is obviously higher in the aged sample based on the calculation and the statistics for numerous TEM images. The average diameter of $L1_2$ nano-particles is estimated to be about 36 and 48 nm for the samples of CRA900 and CRAA900 respectively, which slightly increases after aging. While the average interspacing of $L1_2$ nano-particles is estimated to change from about 100.8 to 25.6 nm after aging, indicating that the relative volume fraction of $L1_2$ phase in the FCC matrix increases significantly from about 10.0% to 20.3% after aging. Thus, both unaged and aged samples show dual heterogeneous structures, but the heterogeneity becomes more severe after aging. Moreover, annealing twins can be observed for both samples. As indicted in Fig. 3c–f for the HRTEM images and the corresponding images after fast Fourier transform (FFT) and inverse FFT, the interfacial coherency can be confirmed, and the $L1_2$ nano-particles are observed to be fully coherent with the FCC matrix, and the diameters are about 40 nm, which is consistent with TEM images.

Tensile properties for the samples annealed at different temperatures have been obtained and been compared with the corresponding samples after aging, to illustrate the aging effect on the tensile properties. The engineering stress-strain curves for the unaged and aged samples are shown in Fig. 4a, in which the curves for the unaged samples are solid lines while the curves for the corresponding aged samples are dash lines. The corresponding true stress-strain curves are displayed in Fig. 4b. The strain hardening rate Θ is plotted as a function of true strain for one typical unaged sample and one typical aged sample in Fig. 4c. The hardening rate is observed to be higher for the aged sample as compared to the corresponding unaged sample, indicating a stronger strain hardening after aging. Both samples show a transient up-turn phenomenon on the hardening rate curves, while the transient up-turn hardening behavior is more obvious for the aged sample as compared to the corresponding unaged sample (the magnitude for the up-turn is higher for the aged sample).

According to previous research [15,31–33], HDI hardening plays a more important role generally at the elasto-plastic deformation stage for heterogeneous structures with various domains with dramatic different strength/hardness, resulting in this transient up-turn hardening behavior and better tensile properties. Thus, the observed higher hardening rate and the more obvious transient up-turn hardening behavior for the aged samples can be attributed to the more severe heterogeneity after aging. Moreover, the plots of yield strength vs. uniform elongation for the unaged and aged samples are displayed in Fig. 4d, along with the data from literatures [12,14,15] for the CrCoNi MEA with both homogeneous and heterogeneous grain structures. It is interesting to note that the tensile properties for the present Co34.5Cr32Ni27.5Al3Ti3 MEA with dual heterogeneous structures are observed to be better than those for the CoCrNi MEA with both homogeneous and heterogeneous grain structures. Moreover, the aged samples display a better synergy of strength and ductility than the corresponding unaged samples, and the corresponding mechanisms will be revealed next.

In the present Co34.5Cr32Ni27.5Al3Ti3 MEA with dual heterogeneous structures, the UFG areas can be considered as hard domains compared to the soft CG areas, while the $L1_2$ nano-particles in the FCC matrix should be considered as even harder nano-domains. As a result, the HDI hardening should play important roles in such dual heterogeneous structures for excellent tensile properties since back and forward stresses can be induced due to the plastic deformation incompatibilities among the soft CG domain, the hard UFG domain and the even harder $L1_2$ nano-domain [15,31–33]. Thus, the LUR tests have been conducted on a typical unaged sample (CRA900) and the corresponding aged sample (CRAA900) in order to reveal and compare the aging effects on the HDI hardening and the tensile properties. The two true stress-strain

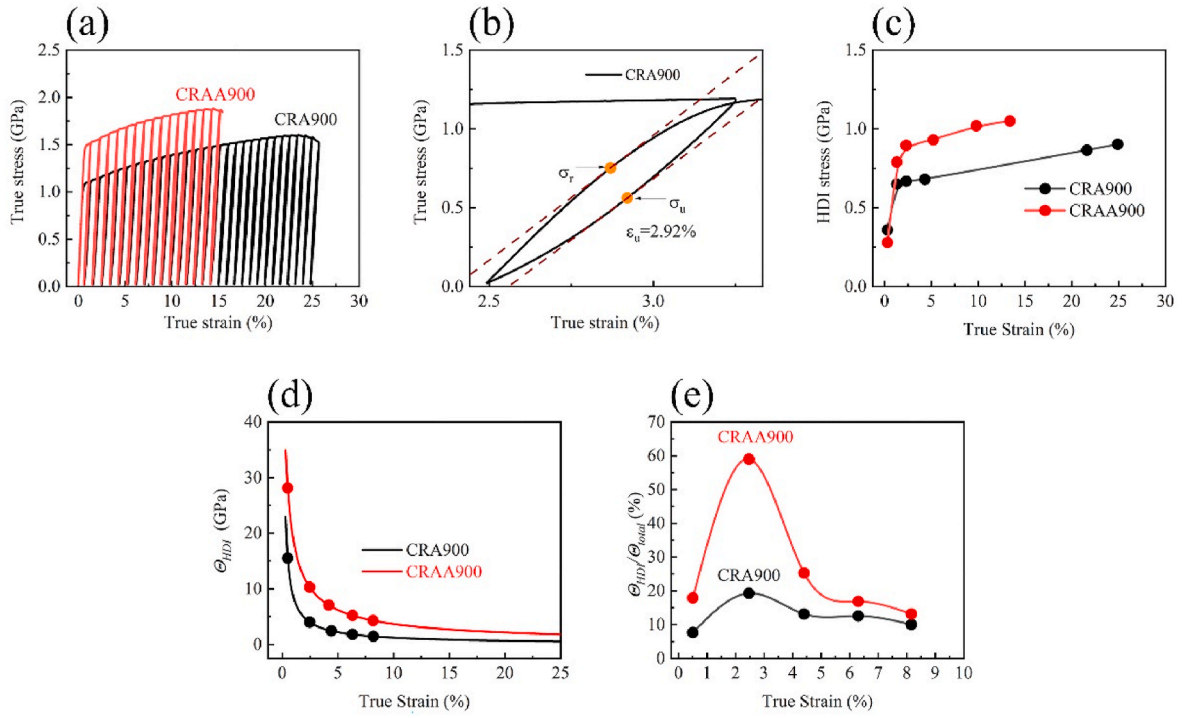

Fig. 5. HDI hardening for one typical unaged sample and one typical aged sample. (a) True stress-strain curves for LUR tests. (b) The typical hysteresis loop at one pre-determined tensile strain. (c) σ_{HDI} as a function of true strain. (d) HDI hardening rate (Θ_{HDI}) as a function of true strain. (e) $\Theta_{\mathrm{HDI}}/\Theta_{\mathrm{total}}$ as a function of true strain.

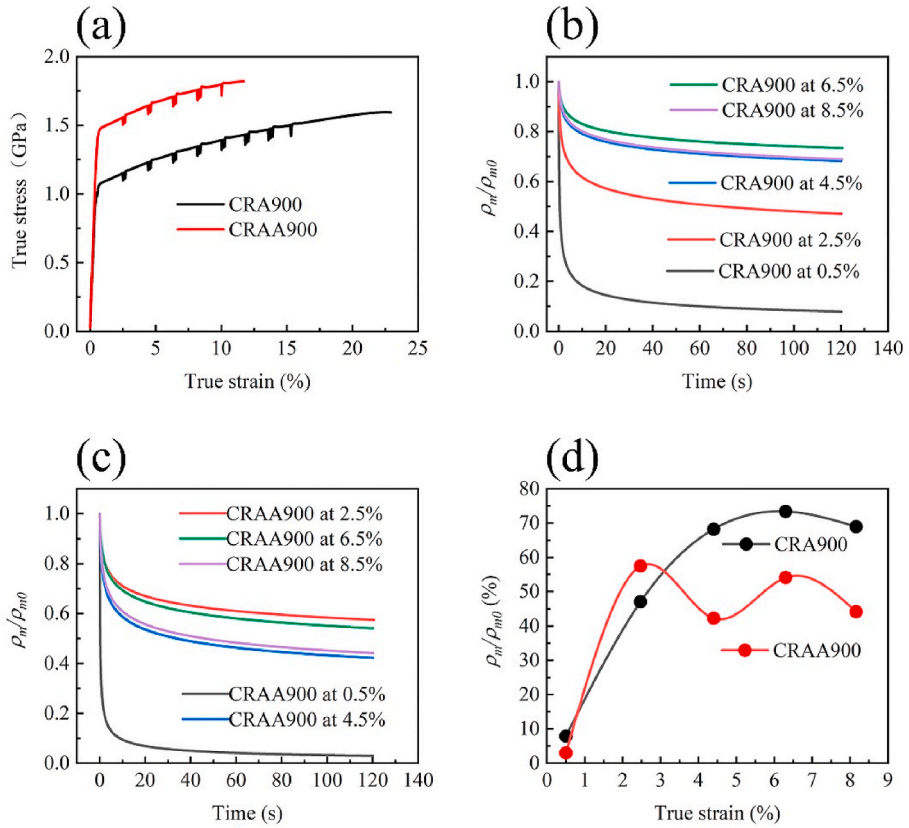

Fig. 6. (a) True stress-strain curves for stress relaxation tests. Evolutions of the mobile dislocation density $\rho_{\mathrm{m}}/\rho_{\mathrm{m0}}$ with time during the first stress relaxation at varying starting strains for (b) one typical unaged sample and (c) one typical aged sample. (d) The steady values of $\rho_{\mathrm{m}}/\rho_{\mathrm{m0}}$ after relaxation as a function of starting tensile strain.

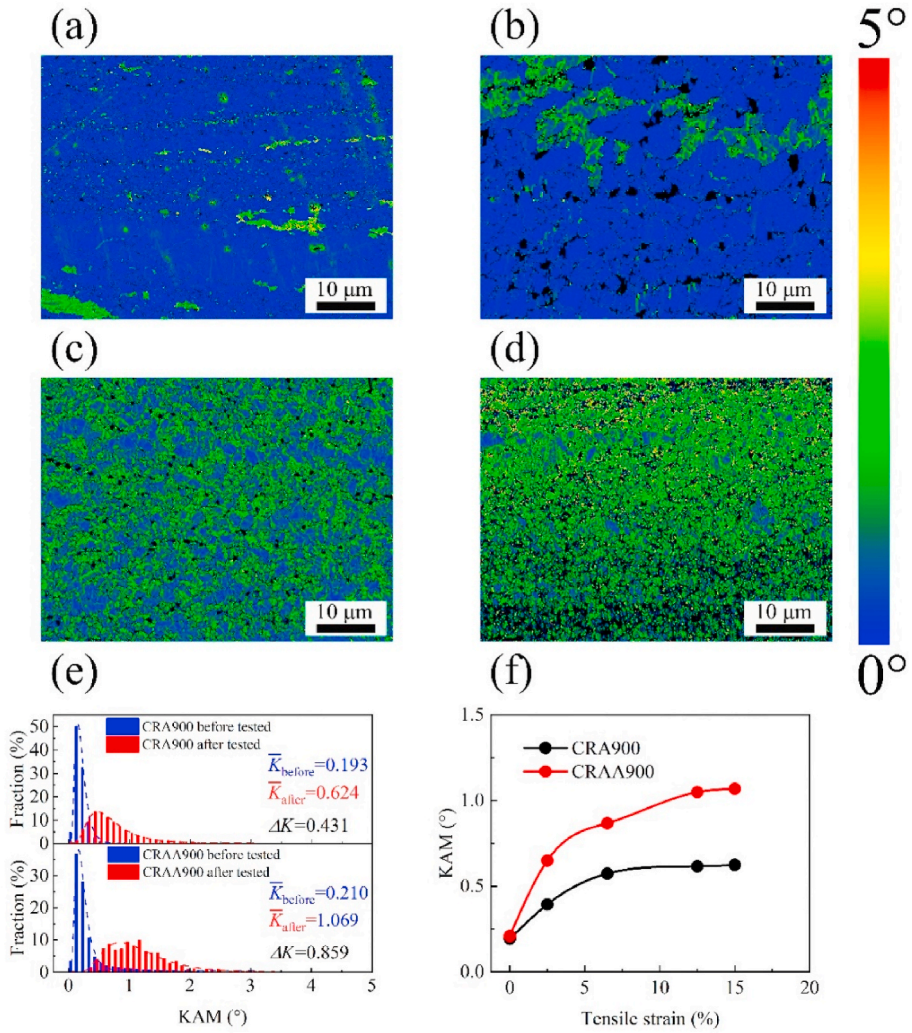

Fig. 7. KAM mappings prior to tensile testing for (a) one typical unaged sample and (b) one typical aged sample. KAM mappings at tensile strain of 15% for (c) one typical unaged sample and (d) one typical aged sample. (e) Histogram distributions of KAM values prior to and after tensile testing (at the same tensile strain of 15%) for both samples. (f) Average KAM values as a function of tensile strain for both samples.

curves for LUR tests are displayed in Fig. 5a. The typical hysteresis loop at one pre-determined tensile strain is shown in Fig. 5b to illustrate the method for the calculations of the unloading and reloading yield stresses (σ_u, σ_r, marked orange circles). The HDI stress (back stress) can be estimated by the following equation: $\sigma_{HDI} = (\sigma_u + \sigma_r)/2$) according to our previous paper [32].

The curves of σ_{HDI} as a function of true strain for these two samples are shown in Fig. 5c. Then, the two curves of HDI hardening rate (Θ_{HDI}) as a function of true strain are displayed in Fig. 5d. It is interesting to note that the aged sample has a higher HDI hardening rate as compared to the corresponding unaged sample, which indicates that the HDI hardening should play a more important role for better tensile properties in the aged samples due to the more severe heterogeneity. Finally, the two curves of $\Theta_{\mathrm{HDI}}/\Theta_{\mathrm{total}}$ as a function of true strain are shown in Fig. 5e. $\Theta_{\mathrm{HDI}}/\Theta_{\mathrm{total}}$ can be considered as the contribution of HDI hardening in the overall hardening. It is clearly indicated that $\Theta_{\mathrm{HDI}}/\Theta_{\mathrm{total}}$ in the aged sample is significantly higher than that in the corresponding unaged sample. Moreover, $\Theta_{\mathrm{HDI}}/\Theta_{\mathrm{total}}$ reaches a maximum point for both samples at a tensile strain of about 2.5%, which is in the elasto-plastic transition stage. This observation is consistent with the transient up-turn hardening behaviors in Fig. 4, indicating that HDI hardening plays a more important role during the elasto-plastic transition stage.

As discussed earlier, the dual heterogeneous structures might have unique ability to enhance the multiplication and interaction of dislocations, especially at the elasto-plastic transition stage. Therefore, the evolutions of mobile dislocations for one typical unaged sample (CRA900) and the corresponding aged sample (CRAA900) were examined through repeated stress relaxation tests. The measured true stress-strain curves from stress relaxation tests for the two samples are shown in Fig. 6a. Then these two curves are analyzed to obtain the evolution of mobile dislocation density based on the method of our previous paper [48]. Fig. 6b and c shows the exhaustion curves of mobile dislocation for these two samples, where the vertical axes ($\rho_{\mathrm{m}}/\rho_{\mathrm{m0}}$) represent the retained fraction of mobile dislocation. Then, retained densities of mobile dislocation at the end of relaxation for the two samples are further plotted as a function of tensile strain in Fig. 6d. It is interesting to note that the densities of mobile dislocations increase quickly to the maximum plateau values for both samples at the elasto-plastic transition stage, which is consistent with the transient up-turn hardening behaviors in Fig. 4 and the maximum points for $\Theta_{\mathrm{HDI}}/\Theta_{\mathrm{total}}$ at a tensile strain of about 2.5% in Fig. 5. These observations indicate that the elasto-plastic transition stage is crucial for the dual heterogeneous structures, since the plastic deformation incompatibilities might be more obvious due to the plastic deformation in the softer domains and the still elastic deformation in the harder domain in this stage.

HDI hardening is generally accommodated by high density of GNDs at the interfaces between hard and soft domains [15,31–33]. GNDs could be induced at the interfaces between the CG area and the harder

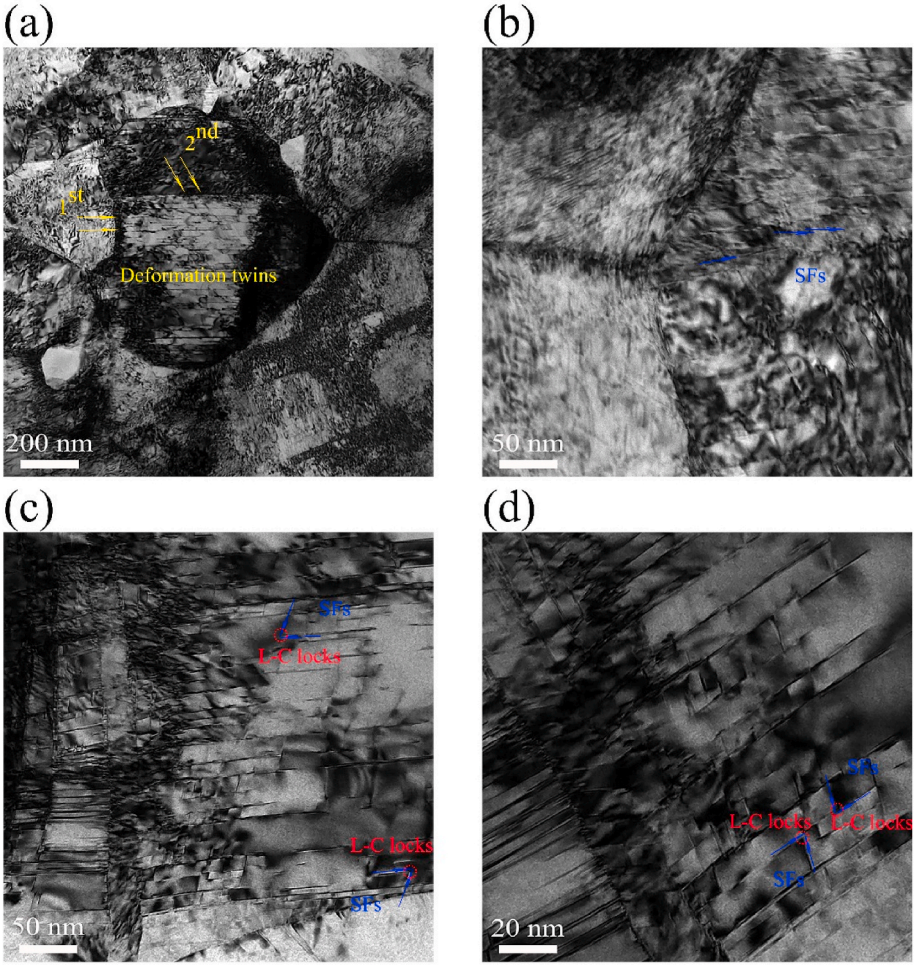

Fig. 8. TEM images after tensile testing for the typical unaged sample. Multiple twins are marked in (a), SFs are indicated in (b), and L-C locks are marked in (c) and (d).

UFG area, and also could be produced at the boundaries of the even harder $L1_2$ nano-domains and the soft FCC matrix in the aforementioned heterogeneous structures. The density of GNDs can generally be obtained using the KAM mapping by a method proposed by Gao and Kubin [50,51], based on the strain gradient theory. Thus, the average KAM values for the KAM mapping can represent the GND density. Thus, the EBSD KAM mappings prior to tensile testing and at a tensile strain of 12.5% for one typical unaged sample (CRA900) and the corresponding aged sample (CRAA900) are displayed in Fig. 7a–d. Then, the histogram distributions of KAM values prior to tensile testing, at a tensile strain of 15% for both samples are shown in Fig. 7e. The average KAM values are plotted as a function of tensile strain in Fig. 7f for both samples. Thus, the increments of the average KAM values after tensile deformation (at the same tensile strain of 15%) for the sample of CRA900 is estimated to be about 0.431^0, while that for the sample of CRAA900 is observed to be much higher (0.859^0). This indicates that the magnitude of strain gradient should have a higher value in the aged samples as compared to the unaged samples due to the more severe heterogeneity in the aged samples, producing higher GND density and resulting in larger HDI hardening for better tensile properties. The average KAM values also increase faster before tensile strain of 6% in both samples, which is also consistent with the transient up-turn hardening behaviors in Fig. 4 and the maximum points for $\Theta_{HDI}/\Theta_{total}$ at a tensile strain of about 2.5% in Fig. 5.

The microstructural deformation mechanisms for the unaged and aged samples have been compared and revealed by TEM observation after tensile testing. The TEM images after tensile testing for the typical unaged sample (CRA900) are shown in Fig. 8. High density of dislocations are observed in the grain interiors after tensile deformation. Moreover, deformation twins, multiple twins, stacking faults (SFs), and formation of Lomer-Cottrell (L-C) locks by partial dislocations from two different inter-crossing (111) planes are also observed for the unaged sample. L-C locks would make the dislocations immobile and also act as barriers of gliding dislocations for strengthening/hardening. These defects can not only reduce the free slip distance of gliding dislocations for strengthening, but also provide adequate pathways for easy glide and cross-slip of dislocations to accommodate plastic deformation for excellent ductility [52–55]. For example, four possible dislocation processes were proposed in the nanotwinned metals [52]: dislocations locks at TBs; SFs associated with TBs; Shockley partial dislocations located at TBs; threading dislocations moving parallel to TBs and confined within twin/matrix lamella. First two mechanisms are immobile and contribute to strengthening/hardening, while last two mechanisms are associated with mobile dislocations to accommodate plastic strain for ductility. By observations from large number of TEM images, no $L1_2$ nano-particles are found after tensile deformation in the typical unaged sample (CRA900). The disappearance of $L1_2$ nano-particles might be due to the shearing mechanism between dislocations and $L1_2$ nano-particles and the low density of $L1_2$ nano-particles in the unaged sample.

It has been indicated earlier that the interspacing becomes smaller and the volume fraction of $L1_2$ nano-particles becomes higher after aging. TEM images after tensile testing for the typical aged sample (CRAA900) are shown in Fig. 9. Dislocations, multiple twins, SFs and L-C locks are observed to form in the grain interior for the aged samples.

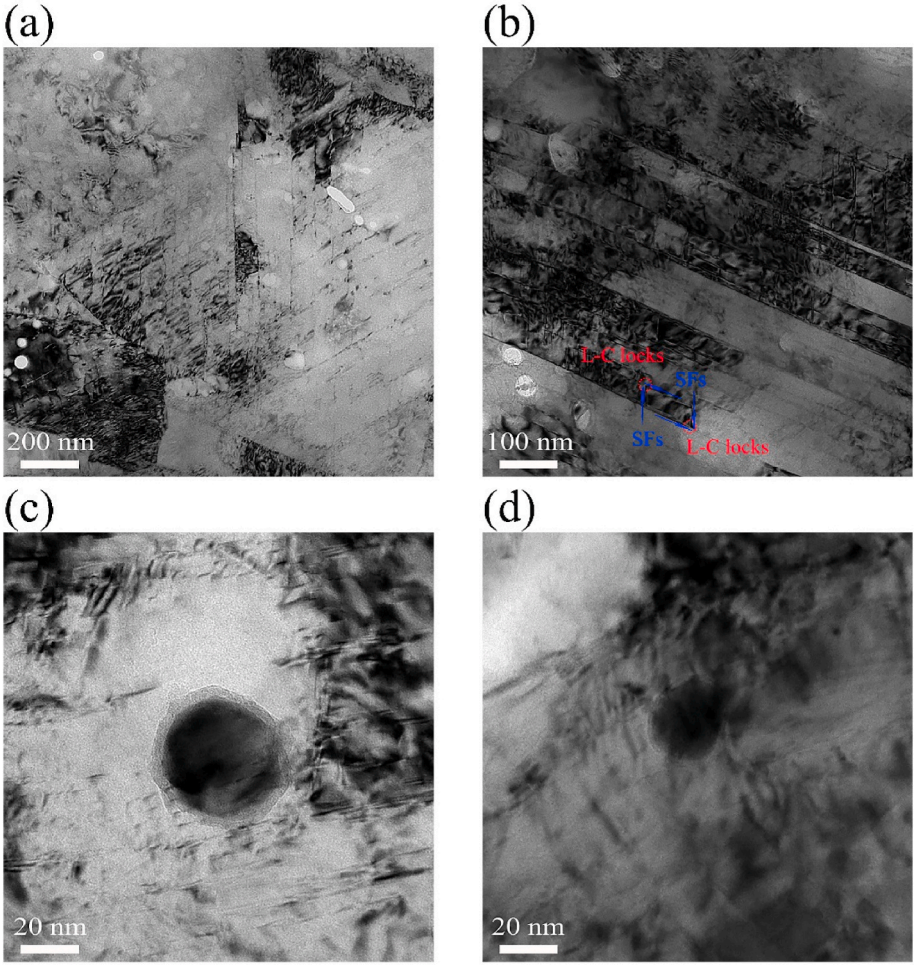

Fig. 9. TEM images after tensile testing for the typical aged sample. L-C locks are indicated in (b).

Moreover, the interactions between these defects (partial dislocations, deformation twins and SFs) and the $L1_2$ nanoprecipitates are also observed due to the much higher density of $L1_2$ nano-particles prior to tensile testing for the aged samples. It is clearly that the $L1_2$ nano-particles can be sheared by these defects, indicating that $L1_2$ nano-particles is strong but deformable. The strong interactions between these defects and $L1_2$ nano-particles should provide additional strain hardening for better tensile properties in the aged samples. The size of $L1_2$ nano-particles is at tens of nm, and the interspacing of $L1_2$ nano-particles is at tens of nm for the unaged sample, the average interspacing is even smaller (100.8–25.6 nm) for the aged sample, the interfacial strain is ultra-low due to the fully coherent interface between the $L1_2$ nano-particles and the FCC matrix, thus these characters of $L1_2$ nano-particles should be effective not only on shearing strengthening/hardening but also on preventing stress concentration at the phase interfaces from early cracks at the phase interfaces.

4. Summaries

In the present study, the CoCrNi-based MEA (Co34.5Cr32-Ni27.5Al3Ti3) has been fabricated to obtain a dual heterogeneous structure with both heterogeneous grain structure and $L1_2$ nano-precipitates by cold rolling, critical annealing and aging. Then the tensile properties and the corresponding deformation mechanisms have been investigated, and the findings can be summarized as follows:

(1) The annealed samples are composed of both heterogeneous grain structure and $L1_2$ nanoprecipitates. The Ni, Ti and Al elements are enriched in the $L1_2$ nanoprecipitates. The size of $L1_2$ nano-precipitates is slightly changed, while the volume fraction of $L1_2$ phase becomes much higher and the corresponding interspacing becomes much smaller after aging, resulting in a more severe heterogeneity.

(2) The tensile properties of the CoCrNi-based MEA with a dual heterogeneous structure are observed to be better than those for the CoCrNi MEA with both homogeneous and heterogeneous grain structures. The aged samples are found to have an even better synergy of strength and ductility than the corresponding unaged samples.

(3) A transient up-turn strain hardening behavior is observed in the dual heterogeneous structures, and this transient hardening behavior is even more obvious in the aged samples than in the unaged samples. HDI hardening is more obvious in the aged samples than in the unaged samples, especially at the elasto-plastic transition stage, producing higher density of GNDs for better tensile properties. Most mobile dislocations are observed to be generated at the elasto-plastic transition stage for both the unaged and aged samples, as indicated by the stress-relaxation tests.

(4) The dominant deformation mechanisms in the unaged samples are multiple deformation twins, SFs and L-C locks, while the interactions between these defects and the $L1_2$ nanoprecipitates provide additional strain hardening mechanisms for the aged samples. The shearing hardening mechanisms are found for the $L1_2$ nanoprecipitates. The $L1_2$ nanoprecipitates are coherent and have size and spacing of tens of nm, which should be very

effective on hardening and on preventing early cracks at phase interfaces. The present results should provide insights for achieving excellent tensile properties in MEAs by architecting dual heterogeneous structures.

Data availability

The raw/processed data required to reproduce these findings cannot be shared at this time due to technical or time limitations.

CRediT authorship contribution statement

Zihan Zhang: Investigation. **Ping Jiang:** Investigation. **Fuping Yuan:** Conceptualization, Writing – original draft, preparation, Supervision. **Xiaolei Wu:** Conceptualization, Supervision.

Declaration of competing interest

The authors declare that they have no known competing financial interests or personal relationships that could have appeared to influence the work reported in this paper.

Acknowledgements

This research was supported by the National Key R&D Program of China [grant number 2017YFA0204402]; the NSFC Basic Science Center Program for "Multiscale Problems in Nonlinear Mechanics" [grant number 11988102], and the Strategic Priority Research Program of the Chinese Academy of Sciences [grant number XDB22040503].

References

[1] J.W. Yeh, S.K. Chen, S.J. Lin, J.Y. Gan, T.S. Chin, T.T. Shun, C.H. Tsau, S.Y. Chang, Nanostructured high-entropy alloys with multiple principal elements: novel alloy design concepts and outcomes, Adv. Eng. Mater. 6 (2004) 299–303.
[2] B. Cantor, I.T.H. Chang, P. Knight, A.J.B. Vincent, Microstructural development in equiatomic multicomponent alloys, Mater. Sci. Eng. 375–377 (2004) 213–218.
[3] E.P. George, D. Raabe, R.O. Ritchie, High-entropy alloys, Nat. Rev. Mater. 4 (2019) 515–534.
[4] B. Gludovatz, A. Hohenwarter, D. Catoor, E.H. Chang, E.P. George, R.O. Ritchie, A fracture-resistant high-entropy alloy for cryogenic applications, Science 345 (2014) 1153–1158.
[5] B. Schuh, F. Mendez-Martin, B. Völker, E.P. George, H. Clemens, R. Pippan, A. Hohenwarter, Mechanical properties, microstructure and thermal stability of a nanocrystalline CoCrFeMnNi high-entropy alloy after severe plastic deformation, Acta Mater. 96 (2015) 258–268.
[6] Z. Li, K.G. Pradeep, Y. Deng, D. Raabe, C.C. Tasan, Metastable high-entropy dual-phase alloys overcome the strength–ductility trade-off, Nature 534 (2016) 227–230.
[7] Y.H. Jo, S. Jung, W.M. Choi, S.S. Sohn, H.S. Kim, B.J. Lee, N.J. Kim, S. Lee, Cryogenic strength improvement by utilizing room-temperature deformation twinning in a partially recrystallized VCrMnFeCoNi high-entropy alloy, Nat. Commun. 8 (2017) 15719.
[8] Z.F. Lei, X.J. Liu, Y. Wu, H. Wang, S.H. Jiang, S.D. Wang, X.D. Hui, Y.D. Wu, B. Gault, P. Kontis, D. Raabe, L. Gu, Q.H. Zhang, H.W. Chen, H.T. Wang, J.B. Liu, K. An, Q.S. Zeng, T.-G. Nieh, Z.P. Lu, Enhanced strength and ductility in a high-entropy alloy via ordered oxygen complexes, Nature 563 (2018) 546–550.
[9] P.J. Shi, W.L. Ren, T.X. Zheng, Z.M. Ren, X.L. Hou, J.C. Peng, P.F. Hu, Y.F. Gao, Y. B. Zhong, P.K. Liaw, Enhanced strength–ductility synergy in ultrafine-grained eutectic high-entropy alloys by inheriting microstructural lamellae, Nat. Commun. 10 (2019) 489.
[10] Q.Q. Ding, Y. Zhang, X. Chen, X.Q. Fu, D.K. Chen, S.J. Chen, L. Gu, F. Wei, H.B. Bei, Y.F. Gao, M.R. Wen, J.X. Li, Z. Zhang, T. Zhu, R.O. Ritchie, Q. Yu, Tuning element distribution, structure and properties by composition in high-entropy alloys, Nature 574 (2019) 223–227.
[11] Z.L. Yang, M.X. Yang, Y. Ma, L.L. Zhou, W.Q. Cheng, F.P. Yuan, X.L. Wu, Strain rate dependent shear localization and deformation mechanisms in the CrMnFeCoNi high-entropy alloy with various microstructures, Mater. Sci. Eng., A 793 (2020) 139854.
[12] B. Gludovatz, A. Hohenwarter, K.V. Thurston, H. Bei, Z. Wu, E.P. George, R. O. Ritchie, Exceptional damage-tolerance of a medium-entropy alloy CrCoNi at cryogenic temperatures, Nat. Commun. 7 (2016) 10602.
[13] J. Miao, C.E. Slone, T.M. Smith, C. Niu, H. Bei, M. Ghazisaeidi, G.M. Pharr, M. J. Mills, The evolution of the deformation substructure in a Ni-Co-Cr equiatomic solid solution alloy, Acta Mater. 132 (2017) 35–48.
[14] S. Yoshida, T. Bhattacharjee, Y. Bai, N. Tsuji, Friction stress and Hall-Petch relationship in CoCrNi equi-atomic medium entropy alloy processed by severe plastic deformation and subsequent annealing, Scripta Mater. 134 (2017) 33–36.
[15] M.X. Yang, D.S. Yan, F.P. Yuan, P. Jiang, E. Ma, X.L. Wu, Dynamically reinforced heterogeneous grain structure prolongs ductility in a medium-entropy alloy with gigapascal yield strength, Proc. Natl. Acad. Sci. U.S.A. 115 (2018) 7224–7229.
[16] Y. Ma, F.P. Yuan, M.X. Yang, P. Jiang, E. Ma, X.L. Wu, Dynamic shear deformation of a CrCoNi medium-entropy alloy with heterogeneous grain structures, Acta Mater. 148 (2018) 407–418.
[17] M.X. Yang, L.L. Zhou, C. Wang, P. Jiang, F.P. Yuan, E. Ma, X.L. Wu, High impact toughness of CrCoNi medium-entropy alloy at liquid-helium temperature, Scripta Mater. 172 (2019) 66–71.
[18] S.S. Sohn, A.K. da Silva, Y. Ikeda, F. Körmann, W. Lu, W.S. Choi, B. Gault, D. Ponge, J. Neugebauer, D. Raabe, Ultrastrong medium-entropy single-phase Alloys designed via severe lattice distortion, Adv. Mater. 31 (2019) 1807142.
[19] C.E. Slone, J. Miao, E.P. George, M.J. Mills, Achieving ultra-high strength and ductility in equiatomic CrCoNi with partially recrystallized microstructures, Acta Mater. 165 (2019) 496–507.
[20] X.L. Wu, M.X. Yang, P. Jiang, C. Wang, L.L. Zhou, F.P. Yuan, E. Ma, Deformation nanotwins suppress shear banding during impact test of CrCoNi medium-entropy alloy, Scripta Mater. 178 (2020) 452–456.
[21] Q.-J. Li, H. Sheng, E. Ma, Strengthening in multi-principle element alloys with local-chemical-order roughened dislocation pathways, Nat. Commun. 10 (2019) 3563.
[22] R.P. Zhang, S.T. Zhao, J. Ding, Y. Chong, T. Jia, C. Ophus, M. Asta, R.O. Ritchie, A. M. Minor, Short-range order and its impact on the CrCoNi medium-entropy alloy, Nature 582 (2020) 283–287.
[23] X.F. Chen, Q. Wang, Z.Y. Cheng, M.L. Zhu, H. Zhou, P. Jiang, L.L. Zhou, Q.Q. Xue, F.P. Yuan, J. Zhu, X.L. Wu, E. Ma, Direct observation of chemical short-range order in a medium-entropy alloy, Nature 592 (2021) 712–716.
[24] Y. Ma, M.X. Yang, F.P. Yuan, X.L. Wu, Deformation induced hcp nano-lamella and its size effect on the strengthening in a CoCrNi medium-entropy alloy, J. Mater. Sci. Technol. 82 (2021) 122–134.
[25] M.L. Hu, W.D. Song, D.B. Duan, Y. Wu, Dynamic behavior and microstructure characterization of TaNbHfZrTi high-entropy alloy at a wide range of strain rate and temperatures, Int. J. Mech. Sci. 182 (2020) 105738.
[26] L. Wang, J.W. Qiao, S.G. Ma, Z.M. Jiao, T.W. Zhang, G. Chen, D. Zhao, Y. Zhang, Z. H. Wang, Mechanical response and deformation behavior of Al0.6CoCrFeNi high-entropy alloys upon dynamic loading, Mater. Sci. Eng., A 727 (2018) 208–213.
[27] A. Mishra, D.J. Benson, Mechanical properties of nanocrystalline materials, Prog. Mater. Sci. 51 (2006) 427–556.
[28] Y.T. Zhu, X.Z. Liao, Retaining ductility, Nat. Mater. 3 (2004) 351–352.
[29] X.L. Wu, Y.T. Zhu, Heterogeneous materials: a new class of materials with unprecedented mechanical properties, Mater. Res. Lett. 5 (2017) 527–532.
[30] T.H. Fang, W.L. Li, N.R. Tao, K. Lu, Revealing extraordinary intrinsic tensile plasticity in gradient nano-grained copper, Science 331 (2011) 1587–1590.
[31] X.L. Wu, M.X. Yang, F.P. Yuan, G.L. Wu, Y.J. Wei, X.X. Huang, Y.T. Zhu, Heterogeneous lamella structure unites ultrafine-grain strength with coarse-grain ductility, Proc. Natl. Acad. Sci. U.S.A. 112 (2015) 14501–14505.
[32] M.X. Yang, Y. Pan, F.P. Yuan, Y.T. Zhu, X.L. Wu, Back stress strengthening and strain hardening in gradient structure, Mater. Res. Lett. 4 (2016) 145–151.
[33] Y.T. Zhu, X.L. Wu, Perspective on hetero-deformation induced (HDI) hardening and back stress, Mater. Res. Lett. 7 (2019) 393–398.
[34] S.-H. Kim, H. Kim, N.J. Kim, Brittle intermetallic compound makes ultrastrong low-density steel with large ductility, Nature 518 (2015) 77–79.
[35] I. Gutierrez-Urrutia, D. Raabe, Influence of Al content and precipitation state on the mechanical behavior of austenitic high-Mn low-density steels, Scripta Mater. 68 (2013) 343–347.
[36] Z.W. Wang, W.J. Lu, H. Zhao, C.H. Liebscher, J.Y. He, D. Ponge, D. Raabe, Z.M. Li, Ultrastrong lightweight compositionally complex steels via dual-nanoprecipitation, Sci. Adv. 6 (2020), eaba9543.
[37] S.H. Jiang, H. Wang, Y. Wu, X.J. Liu, H.H. Chen, M.J. Yao, B. Gault, D. Ponge, D. Raabe, A. Hirata, M.W. Chen, Y.D. Wang, Z.P. Lu, Ultrastrong steel via minimal lattice misfit and high-density nanoprecipitation, Nature 544 (2017) 460–464.
[38] J.Y. He, H. Wang, H.L. Huang, X.D. Xu, M.W. Chen, Y. Wu, X.J. Liu, T.G. Nieh, K. An, Z.P. Lu, A precipitation-hardened high-entropy alloy with outstanding tensile properties, Acta Mater. 102 (2016) 187–196.
[39] Z.G. Wang, W. Zhou, L.M. Fu, J.F. Wang, R.C. Luo, X.C. Han, B. Chen, X.D. Wang, Effect of coherent L12 nanoprecipitates on the tensile behavior of a fcc-based high-entropy alloy, Mater. Sci. Eng. 696 (2017) 503–510.
[40] T. Yang, Y.L. Zhao, Y. Tong, Z.B. Jiao, J. Wei, J.X. Cai, X.D. Han, D. Chen, A. Hu, J. J. Kai, K. Lu, Y. Liu, C.T. Liu, Multicomponent intermetallic nanoparticles and superb mechanical behaviors of complex alloys, Science 362 (2018) 933–937.
[41] Y.J. Liang, L.J. Wang, Y.R. Wen, B.Y. Cheng, Q.L. Wu, T.Q. Cao, Q. Xiao, Y.F. Xue, G. Sha, Y.D. Wang, Y. Ren, X.Y. Li, L. Wang, F.C. Wang, H.N. Cai, High-content ductile coherent nanoprecipitates achieve ultrastrong high-entropy alloys, Nat. Commun. 9 (2018) 4063.
[42] Y.Y. Zhao, H.W. Chen, Z.P. Lu, T.G. Nieh, Thermal stability and coarsening of coherent particles in a precipitation-hardened (NiCoFeCr)94Ti2Al4 high-entropy alloy, Acta Mater. 147 (2018) 184–194.
[43] K.S. Ming, X.F. Bi, J. Wang, Realizing strength-ductility combination of coarse-grained Al0.2Co1.5CrFeNi1.5Ti0.3 alloy via nano-sized, coherent precipitates, Int. J. Plast. 100 (2018) 177–191.
[44] T. Yang, Y.L. Zhao, J.H. Luan, B. Han, J. Wei, J.J. Kai, C.T. Liu, Nanoparticles-strengthened high-entropy alloys for cryogenic applications showing an exceptional strength-ductility synergy, Scripta Mater. 164 (2019) 30–35.

[45] Y. Ma, J.M. Hao, J.C. Jie, Q. Wang, C. Dong, Coherent precipitation and strengthening in a dual-phase AlNi2Co2Fe1.5Cr1.5 high-entropy alloy, Mater. Sci. Eng. 764 (2019) 138241.
[46] X.H. Du, W.P. Li, H.T. Chang, T. Yang, G.S. Duan, B.L. Wu, J.C. Huang, F.R. Chen, C.T. Liu, W.S. Chuang, Y. Lu, M.L. Sui, E.W. Huang, Dual heterogeneous structures lead to ultrahigh strength and uniform ductility in a Co-Cr-Ni medium-entropy alloy, Nat. Commun. 11 (2020) 2390.
[47] Y. Yang, T.Y. Chen, L.Z. Tan, J.D. Poplawsky, K. An, Y.L. Wang, G.D. Samolyuk, K. Littrell, A.R. Lupini, A. Borisevich, E.P. George, Bifunctional nanoprecipitates strengthen and ductilize a medium-entropy alloy, Nature 595 (2021) 245–249.
[48] X.L. Wu, P. Jiang, L. Chen, F.P. Yuan, Y.T. Zhu, Extraordinary strain hardening by gradient structure, Proc. Natl. Acad. Sci. Unit. States Am. 111 (2014) 7197–7201.
[49] F.P. Yuan, Strengthening effects of various grain boundaries with nano-spacing as barriers of dislocation motion from molecular dynamics simulations, Sci. China Phys. Mech. Astron. 60 (2017), 034611.
[50] H.J. Gao, Y.G. Huang, W.D. Nix, J.W. Hutchinson, Mechanism-based strain gradient plasticity - I. Theory, J. Mech. Phys. Solid. 47 (1999) 1239–1263.
[51] L.P. Kubin, A. Mortensen, Geometrically necessary dislocations and strain-gradient plasticity: a few critical issues, Scripta Mater. 48 (2003) 119–125.
[52] L. Lu, Z.S. You, K. Lu, Work hardening of polycrystalline Cu with nanoscale twins, Scripta Mater. 66 (2012) 837–842.
[53] L.L. Zhu, S.X. Qu, X. Guo, J. Lu, Analysis of the twin spacing and grain size effects on mechanical properties in hierarchically nanotwinned face-centered cubic metals based on a mechanism based plasticity model, J. Mech. Phys. Solid. 76 (2015) 162–179.
[54] L. Dupuy, M.C. Fivel, A study of dislocation junctions in FCC metals by an orientation dependent line tension model, Acta Mater. 50 (2002) 4873–4885.
[55] W.W. Jin, G.M. Cheng, W.Z. Xu, H. Yuan, M.H. Tsai, Q.D. Wang, C.C. Koch, Y. T. Zhu, S.N. Mathaudhu, Ultrastrong Mg alloy via nano-spaced stacking faults, Mater. Res. Lett. 1 (2013) 61–66.